

Article

# Unraveling the Mechanism for H<sub>2</sub>O<sub>2</sub> Photogeneration on Polymeric Carbon Nitride with Alkali Metal Modification

Zehao Li <sup>1,2,\*</sup> and Yufei Chen <sup>2</sup>

<sup>1</sup> Guangdong Provincial Key Laboratory of Chemical Measurement and Emergency Test Technology, Institute of Analysis, Guangdong Academy of Sciences (China National Analytical Center, Guangzhou), Guangzhou 510070, China

<sup>2</sup> School of Chemistry and Chemical Engineering, Anyang Normal University, Anyang 455000, China

\* Correspondence: zehaoli512@outlook.com

**Abstract:** K and Na have been widely used in photocatalytic H<sub>2</sub>O<sub>2</sub> production. However, Rb and Cs have rarely been studied for their photocatalytic potentials. In addition, the mechanism regulating H<sub>2</sub>O<sub>2</sub> production from different alkali metal (M)-modified polymeric carbon nitride (PCN) is still unknown. Therefore, M-doped PCN was fabricated using thermal copolymerization in the presence of Li, Na, K, Rb, or Cs. The activity of CN-M was enhanced by the increase in the metallic character of alkali metals. However, CN-Cs's photocatalytic H<sub>2</sub>O<sub>2</sub> activity is not optimal even though it has the strongest metallic character. A stronger metallic character is anticipated to yield stronger Lewis acidic sites. Although ethanol can be adsorbed and activated at strong Lewis acidic sites, H<sub>2</sub>O<sub>2</sub> can also be activated at these sites, which speeds up H<sub>2</sub>O<sub>2</sub> degradation. CN-Rb—with its acceptable metallic character, excellent oxygen adsorption capacity, and reduced H<sub>2</sub>O<sub>2</sub> degradation—has the best photocatalytic H<sub>2</sub>O<sub>2</sub> yield.

**Keywords:** carbon nitride; hydrogen peroxide; photocatalysis; alkali metals



**Citation:** Li, Z.; Chen, Y. Unraveling the Mechanism for H<sub>2</sub>O<sub>2</sub> Photogeneration on Polymeric Carbon Nitride with Alkali Metal Modification. *Catalysts* **2023**, *13*, 218. <https://doi.org/10.3390/catal13020218>

Academic Editors: Zhongzhe Wei and Yutong Gong

Received: 30 December 2022

Revised: 13 January 2023

Accepted: 16 January 2023

Published: 17 January 2023



**Copyright:** © 2023 by the authors. Licensee MDPI, Basel, Switzerland. This article is an open access article distributed under the terms and conditions of the Creative Commons Attribution (CC BY) license (<https://creativecommons.org/licenses/by/4.0/>).

## 1. Introduction

Hydrogen peroxide (H<sub>2</sub>O<sub>2</sub>) is an essential inorganic chemical that has been extensively employed in organic syntheses, environmental remediations, paper pulp bleaching, and medical disinfection [1–4]. Being an environmentally friendly technique, photocatalytic H<sub>2</sub>O<sub>2</sub> generation has recently attracted wider scientific attention as a topic [5–9]. In particular, polymeric carbon nitride (PCN) has received greater scientific attention for its potential to produce H<sub>2</sub>O<sub>2</sub> by photocatalysis. This is likely because PCN has a high selectivity for this reaction and can easily change its morphology, molecular structure, and band gap [2,10,11].

Various techniques have been employed for the modification of PCN for photocatalytic H<sub>2</sub>O<sub>2</sub> generation. Molecular doping [12], morphological or defect engineering [13], and the construction of composite semiconductors [14,15] are currently the key research areas for the modification of PCN for photocatalytic H<sub>2</sub>O<sub>2</sub> generation. Notably, there are a number of research studies on alkali metal ions, such as K<sup>+</sup> and Na<sup>+</sup> [16,17]. For example, Wang et al. obtained CNK<sub>0.2</sub> containing N vacancies by calcining KOH and supramolecules [18]. The more negative charge on the surface of CNK<sub>0.2</sub> improves its capacity to adsorb oxygen and, as a result, increases the production of photocatalytic H<sub>2</sub>O<sub>2</sub>, under the impact of N vacancy. Due to the synergistic effects of doping and defect, K<sup>+</sup>/Na<sup>+</sup>-doped PCN fabricated by Wu et al., demonstrated good photocatalytic H<sub>2</sub>O<sub>2</sub> generation [19]. By using KOH and melamine to modify PCN, Zhang et al. created a material that increased electron transport owing to the existence of a K bridge between the C<sub>3</sub>N<sub>4</sub> layers and had a great ability to attract electrons due to a N defect formed by a cyano group and a vacancy [20]. K intercalation produced Lewis acidic sites for isopropanol adsorption and enhanced Lewis basic sites for proton release and hydrogen abstraction in PCN with Lewis acidic–basic sites

prepared by Long et al. [17]. Liu et al. prepared oxygen- and potassium-dual-heteroatom-incorporated PCN, which demonstrated a significantly improved photocatalytic  $\text{H}_2\text{O}_2$  production [21].  $\text{Na}^+$  doping has also been thoroughly investigated. With cyano groups and Na dopants, Chen et al. created a porous PCN with improved photocatalytic activity (7.01 mM/h under visible light) [22]. Zhao et al. discovered that the pyridinic nitrogen-coordinated sodium and cyanamino group in the PCN modified with NaSCN led to better charge separation efficiency, increased surface adsorption of  $\text{O}_2$ , and produced surface-active sites for  $2\text{e}^-$ -oxygen-reduction reaction [16]. The above research shows that the introduction of K or Na alkali metal ions can greatly improve the  $\text{H}_2\text{O}_2$  production activity of modified PCN. Among alkali metals, there are, however, only a few studies on the modification of PCN with Li, Rb, or Cs, and it is important to investigate if these modifications are similarly efficient and also what the essential mechanism regulating their function is.

Therefore, in this work, Li, Na, K, Rb, and Cs alkali metal ions were introduced into the structure of PCN via elemental doping, and the optimal addition amount of each metal ion was optimized. By measuring their photocatalytic  $\text{H}_2\text{O}_2$  production activities, the order of influence of the above five ions on the photocatalytic performance was determined. A series of characterization methods, such as TPD- $\text{NH}_3$  and TPD- $\text{O}_2$ , were used to examine the influence of the five ions on the photocatalytic activity. For the modified PCN, metallicity, oxygen and alcohol adsorption, and activation ability on the catalyst surface are the key factors affecting photocatalytic  $\text{H}_2\text{O}_2$  production. Finally, it was concluded that Rb ion—on account of its appropriate metallic character, Lewis acidic activity intensity, excellent oxygen and alcohol adsorption, and activation ability—had the best photocatalytic performance. This paper provides a useful foundation for further investigating the photocatalytic reactions of alkali metal ion-modified PCN.

## 2. Results and Discussion

### 2.1. Morphology and Chemical Structures

The obtained PCN's morphological characteristics were determined via SEM. All samples, as seen in Figure S1, have asymmetrical forms and lack any unique morphology or structure. Table S1 and Figure S2 show the  $\text{N}_2$  sorption–desorption isotherms and pore size distribution curves of the acquired PCN specimens. The modified PCN's particular surface areas are not much larger than those of CN. The specific surface areas of CN-Cs, CN-K, and CN-Rb, on the other hand, decrease, which might be caused by the addition of metal ions and the filling of the holes. The short metallic atomic radius of CN-Li and CN-Na may be the cause of the minor rise in their specific surface areas. The same pattern can also be seen in the plots of the pore size distribution (Figure S2b). The results show that improving photocatalytic activity in this work was not primarily influenced by the particular surface area of modified PCN.

Measurements of XRD spectra, FT-IR patterns, and XPS spectra were made to acquire an understanding of PCN structures. Two diffraction peaks at  $12.83^\circ$  and  $27.40^\circ$ , corresponding to the (100) and (002) planes of PCN, were observed for the CN specimen, as depicted in Figure 1a. The first peak was the interlayer heptazine motif periodic array, while the second peak was the interlayer aromatic packing structure [23]. As for CN-Na, CN-K, and CN-Rb, the diffraction peak at  $12.83^\circ$  disappeared, illustrating that the in-plane packing structure was destroyed [18]. The periodic array of 100 interlayer heptazine motifs' diffraction peak for CN-K and CN-Rb shifts to  $7.78^\circ$  [17,24]. Additionally, the formation of the poly(heptazine imide) structure was indicated by the appearance of two additional peaks in the CN-Li, CN-Rb, and CN-Cs spectra at  $21^\circ$  and  $32^\circ$ , corresponding to the 210 and 310 planes, respectively [25,26]. The metallic character of Li is the lowest among these metals, but the structure of CN-Li was similar to that of CN-Rb, which may be due to the high addition of Li. When preparing the catalyst, the optimal addition amount of each metal was explored, as shown in Table S1. To confirm the above speculation, the XRD

pattern of CN-Li-0.5 was measured (shown in Figure S3). The structure of CN-Li-0.5 was similar to CN-Na, which means that the above speculation is correct.

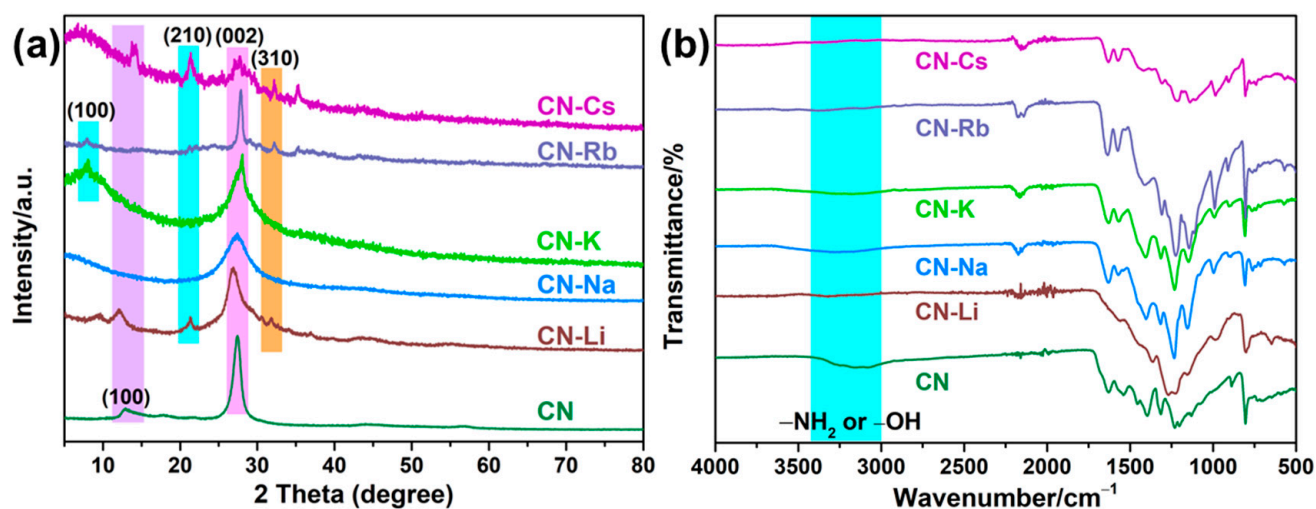
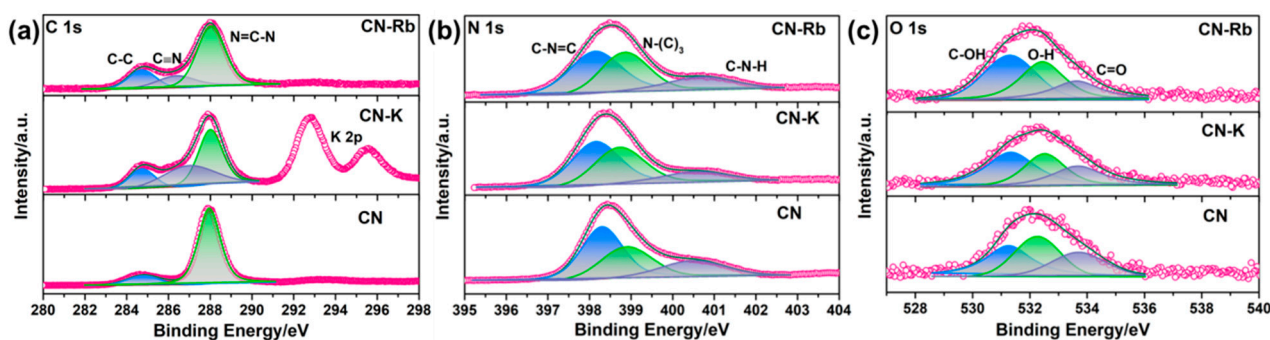


Figure 1. (a) XRD patterns of PCN. (b) FT-IR of PCN.

The resulting PCN's FT-IR spectra (Figure 1b) display structures that are similar to typical PCN characteristic peaks. Notably, the O–H or N–H stretching vibrations of uncondensed  $\text{-NH}_2$  or adsorbed  $\text{H}_2\text{O}$  on the surface correlate to the broadband in the  $2800\text{--}3600\text{ cm}^{-1}$  area [27]. The stretching vibration of the triazine ring and vibration of the C–N heterocycle skeleton, respectively, were attributed to the peaks at  $1100\text{--}1800\text{ cm}^{-1}$  and  $805\text{ cm}^{-1}$ . The CN-M spectra also showed new peaks at  $2000\text{--}2250\text{ cm}^{-1}$  [28], which were ascribed to  $\text{-C}\equiv\text{N}$  stretching vibrations, while the peak strength at  $2800\text{--}3200\text{ cm}^{-1}$  becomes weaker. These findings suggested that some uncondensed  $\text{-NH}_2$  on the surface of PCN had been partially replaced by  $\text{-C}\equiv\text{N}$ . In the CN-M spectra, a brand-new peak at  $989\text{ cm}^{-1}$  was also discovered and was considered to arise from the C–O–H group's stretching vibration [29]. The findings suggest that the CN-M surface included a substantial number of hydrophilic groups, which may have improved the dispersion of the specimen in water.

To investigate the variations in PCN's chemical states, an XPS analysis was conducted. The XPS survey spectra of CN-M showed that C, N, O, and M were present (Figure S4a). Additionally, the high-resolution C 1s, N 1s, and O 1s XPS spectra of the PCNs revealed that they have similar peak shapes (Figures 2 and S4). The two typical peaks for C 1s at 288.2 and 284.8 eV were respectively ascribed to  $\text{N-C=N}$  and C–C [30]. A new peak that was assigned to CN at 286.5 eV may also be seen in the C 1s spectra of CN-M when compared to  $\text{C}\equiv\text{N}$ .  $\text{N-(C)}_3$  bridging N atoms,  $\text{sp}^2$ -bonded N atoms within triazine rings (C–N=C), and C–N–H, are respectively indexed to the three typical peaks in N 1s spectra (Figures 2b and S4c) at 399.1, 398.6, and 400.7 eV [31]. The high-resolution O 1s spectra of CN and CN-M have been shown in Figures 2c and S4d. The spectra of CN and CN-M show three peaks at 531.1, 532.4, and 533.3 eV, attributed to C–O–H and O–H of the water absorbed and C=O, respectively [32,33]. In addition, chloride ion content is negligible in CN-M (as shown in Table S2). Meanwhile, the mole percentage of M has also been listed in Table S2, indicating that M ions are successfully introduced into the CN-M structure.



**Figure 2.** (a) High-resolution XPS spectra of C 1s of obtained PCN. (b) High-resolution XPS spectra of N 1s of obtained PCN. (c) High-resolution XPS spectra of O 1s of obtained PCN.

According to these findings, the addition of M causes the formation of a cyano group at the triazine ring's terminal position, which can be utilized as an inhibitor to stop PCN from polymerizing. The resulting CN-M, however, provides numerous edge active sites with  $-\text{C}\equiv\text{N}$  and  $-\text{OH}$  groups, including CN-K, CN-Rb, and CN-Cs, while maintaining the PCN structure. It indicates that CN-K, CN-Rb, and CN-Cs have better hydrophilicity, which is helpful for aqueous phase dispersion. The findings of free deposition and contact angle experiments provide evidence for the aforementioned conclusion, as depicted in Figures S5 and S6.

## 2.2. Optical and Photoelectrochemical Properties

Figure 3a displays the spectra of CN and CN-M's UV-Vis absorption. In the intrinsic absorption margin, CN-M shows an apparent redshift in comparison to CN, and its absorption property is improved in the visible area, which helps absorb and use visible light. The acquired results have been displayed in Figure 3b and Table S1 after the bandgaps of the various specimens were determined from the UV-Vis absorption spectra. A narrower bandgap ( $E_g$ ) for CN-M than for CN (2.74 eV) renders it convenient for electrons to transition to the conduction band from the valence band.

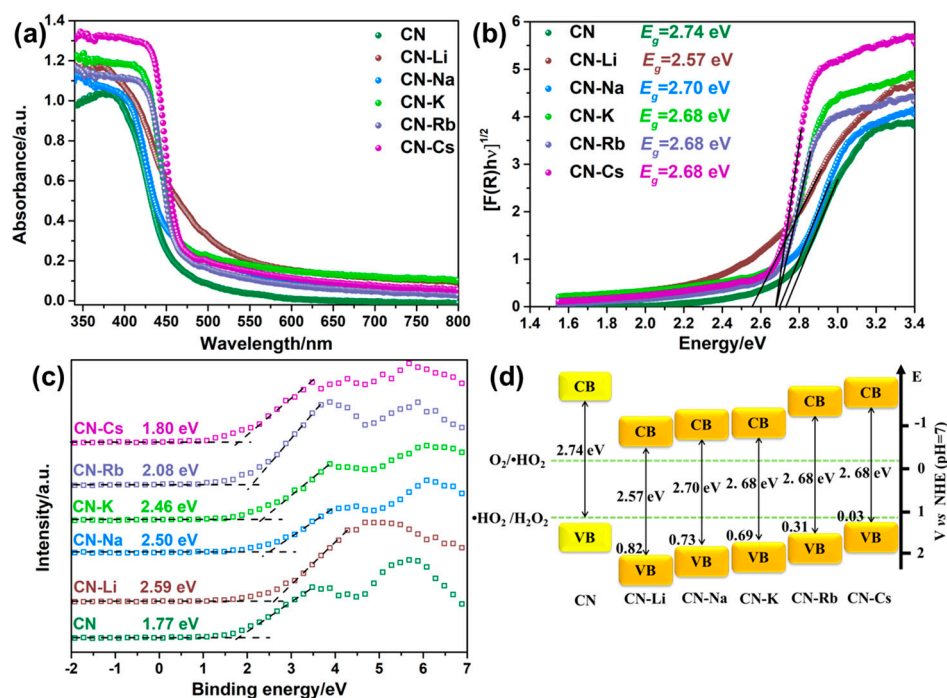


**Figure 3.** (a) DRS spectra of CN and CN-M. (b) The Kubelka-Munk plots of CN and CN-M. (c) XPS valence band spectra. (d) Electronic energy band positions of CN and CN-M.

The specific band locations of CN and CN-M can be identified from the Mott-Schottky (M-S) plot and XPS-VB spectrum (VB) data. First, the *n*-type feature of the semiconductors is revealed by the positive slope in the M-S plots of CN and CN-M (Figure S8) [34]. The photocatalytic reduction reaction benefits from the higher electron concentration found in CN-M, as evidenced by the fact that the CN-M slope is low in comparison to that of CN [34]. Combining with the XPS-VB spectra, the VB value (eV) can be estimated with the equation  $E_V = \Phi + VB_{\max} - 4.44$  at pH = 7 versus the normal hydrogen electrode, where  $\Phi$  is the analyzer's electron-work function (3.88 eV) and  $VB_{\max}$  is the VB maximum that can be obtained from the XPS-VB spectrum. As shown in Figure 3c, the  $VB_{\max}$  value of CN is 1.77 eV. Consequently, the VB value of CN is 1.21 eV. The CN and CN-M bandgaps have been illustrated in Figure 3d. Both are thermodynamically satisfied for  $2e^-$ -ORR.

To examine the charge recombination behavior, the steady-state and time-resolved PL spectroscopies of CN and CN-M were put to the test. Because of the synergistic interaction between the improved transport of electrons between the PCN layers caused by the M bridges and the strong electron-withdrawing capability of the cyano group, as shown in Figure 4a, the CN-M specimens demonstrate substantially less PL emission than CN, suggesting lower charge recombination. In addition, time-resolved transient PL spectroscopy was used to examine the average charge-carrier lifetime and the behaviors of charge-carrier separation. The decay curves were fitted by using the triexponential function. The average charge-carrier lifespan rose from 2.10 ns for CN to 17.95 ns for CN-Rb, as shown in Figure 4b and Table S1, demonstrating that more photogenerated carriers can transfer to its surface to be involved in the reactions occurring on the surface. Additionally, different degrees of advancement had been made in the typical charge-carrier lifetimes of CN-Li, CN-Na, CN-K, and CN-Cs.

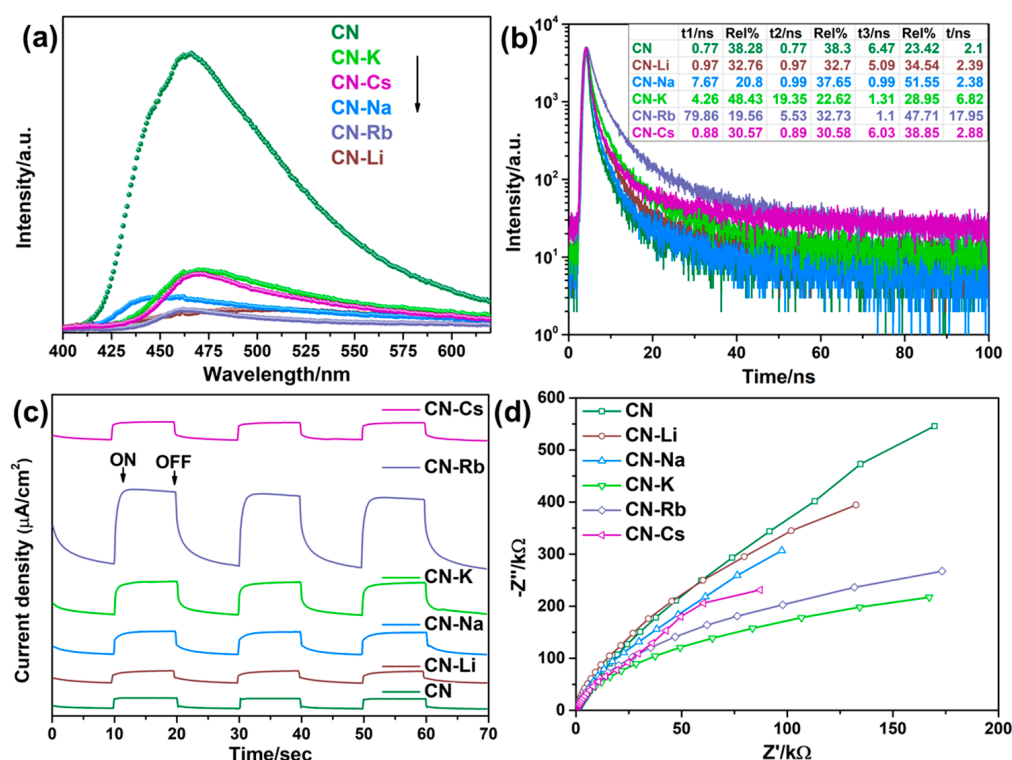


**Figure 4.** (a) Photoluminescence (PL) emission spectra. (b) Fluorescence lifetime decay curves. (c) Periodic on/off photocurrent response in 0.5 M  $Na_2SO_4$  electrolyte under  $\lambda > 420$  nm visible light irradiation at 0.5 V vs. Ag/AgCl electrode. (d) Electrochemical impedance spectra (EIS) plots of CN and CN-M.

Transient photocurrent–time and Nyquist plots for the collected PCN specimens were analyzed. The photocurrent density of CN-Rb is 1.76 A/cm<sup>2</sup>, 7.04 times more than that

of CN ( $0.25 \text{ A/cm}^2$ ) as shown in Figure 4c and Table S1. Further evidence supporting the observation that the modified PCN with alkali metal ions exhibits a more effective interface transfer and separation of charge carriers, comes from the higher photocurrent densities of CN-Li, CN-Na, CN-K, and CN-Cs. In addition, the semicircular curve radius in the CN-M Nyquist plot (Figure 4d) is smaller than that in CN, suggesting that the CN-M has a lower charge transfer resistance than CN. The results show that cyano groups and M dopants can significantly increase light absorption and encourage charge separation.

### 2.3. Photocatalytic Activity

The acquired samples' photocatalytic activity for the generation of  $\text{H}_2\text{O}_2$  was assessed under white LED light. All of the samples display  $\text{H}_2\text{O}_2$  production performances following 60 min of irradiation, as shown in Figure 5a. In particular, the amount of  $\text{H}_2\text{O}_2$  produced by CN was much lower than that of CN-M samples, at just  $59.20 \mu\text{mol/g}$ . The  $\text{H}_2\text{O}_2$  production by CN-M increased with an increasing metallic character from Li to Rb. It then decreased for CN-Cs. Therefore, in comparison to CN, 14.11 times more  $\text{H}_2\text{O}_2$  ( $835.51 \mu\text{mol/g}$ ) was generated by CN-Rb. Additionally, under visible light ( $\lambda > 420 \text{ nm}$ ), the time-dependent variation in the  $\text{H}_2\text{O}_2$  generation rates of CN and CN-M was evaluated. Figure S9 demonstrates that with CN-M, sustained  $\text{H}_2\text{O}_2$  production is seen within 12 h without degradation. The  $\text{H}_2\text{O}_2$  yield of CN-Rb is  $12.52 \text{ mmol/g}$  after 12 h of exposure, which is 156.04 times greater than that of CN ( $80.21 \mu\text{mol/g}$ ). In addition, after 12 h of irradiation, the  $\text{H}_2\text{O}_2$  yields of CN-K and CN-Cs are  $9.10$  and  $8.54 \text{ mmol/g}$ , respectively, indicating that CN-K, CN-Rb, and CN-Cs have outstanding long-term stability. The reaction solution's dissolved oxygen content (DO) was measured at 1 atm,  $\sim 9.82 \text{ mg/L}$ , and  $283.15 \text{ K}$ . The yield of  $\text{H}_2\text{O}_2$  in a  $200 \text{ mL}$  solution should be  $61.37 \mu\text{mol}$  if all oxygen is converted to  $\text{H}_2\text{O}_2$ . The  $\text{H}_2\text{O}_2$  yields of CN-Rb, CN-K, and CN-Cs in our experiment exceeded the theoretical value by  $82.60$ ,  $65.96$ , and  $66.77 \mu\text{mol}$ , respectively, at 1 h.  $\text{H}_2\text{O}_2$  output grew steadily throughout the reaction, showing that  $\text{O}_2$  from the air supplemented the  $\text{O}_2$  in the reaction's solution. This is likely because CN-Rb, CN-K, and CN-Cs have strong  $\text{O}_2$  adsorption capabilities. The performance stabilities of CN-Rb, CN-K, and CN-Cs were assessed by a cycling  $0.03 \text{ g}$  specimen that was washed following centrifugation from the reacted solution (Figure 5b). As a result of the increased reaction time, the  $\text{H}_2\text{O}_2$  yield did not demonstrate any substantial reduction, suggesting outstanding stability for photocatalytic  $\text{H}_2\text{O}_2$  production.

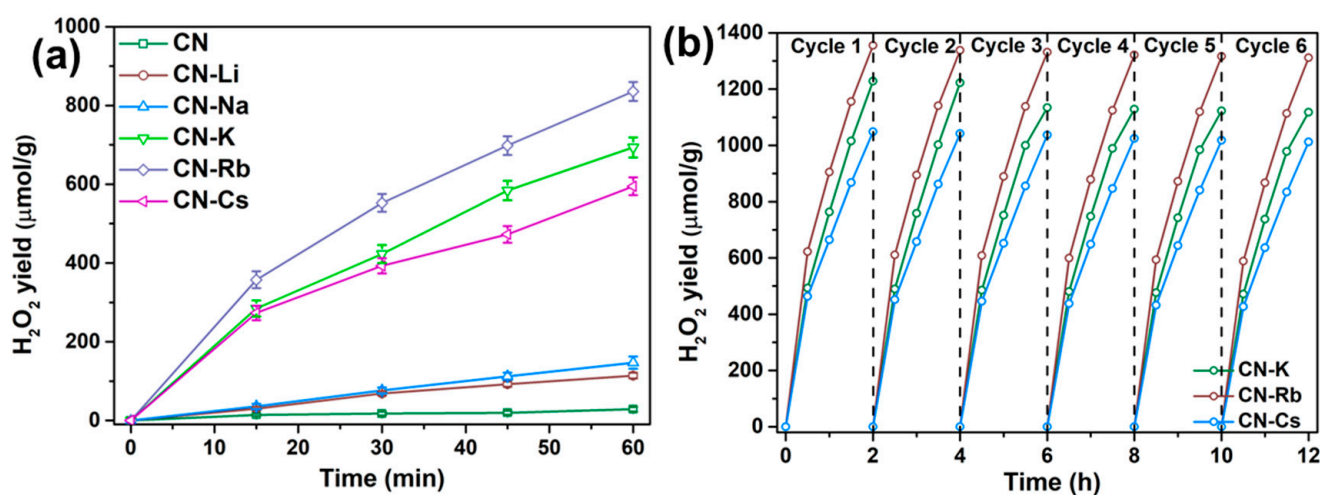


**Figure 5.** (a) Photocatalytic production of  $\text{H}_2\text{O}_2$  by the obtained specimens under white LED light. (b) Time course of the generation of  $\text{H}_2\text{O}_2$  employing CN-K, CN-Rb, and CN-Cs under white LED light.

Moreover, the activity changes of modified PCN obtained by different preparation methods were explored. Melem-M was prepared by calcining melem with MCl. As shown in Figure S10a, compared to CN-M, melem-M shows a similar trend, except that the activity of melem-K was slightly better than that of melem-Rb. This result shows that the order of influence of alkali metal ions on PCN activity is Rb, K, Cs, Na, Li. The photocatalytic H<sub>2</sub>O<sub>2</sub> generation of CN with RbCl or KCl was also carried out to confirm the impact of stray Rb<sup>+</sup> or K<sup>+</sup> on performance. Figure S10b,c demonstrate that the H<sub>2</sub>O<sub>2</sub> yields for CN with various RbCls or KCls are comparable, demonstrating that stray Rb<sup>+</sup> or K<sup>+</sup> does not facilitate photocatalytic H<sub>2</sub>O<sub>2</sub> synthesis. In addition, the photocatalytic decomposition of H<sub>2</sub>O<sub>2</sub> for the samples was tested. In contrast to CN, Figure S10d demonstrates that CN-Li and CN-Na may effectively prevent the breakdown of H<sub>2</sub>O<sub>2</sub> because the amine entities in the PCN edge have been swapped out for cyano groups. Furthermore, CN-K, CN-Rb, and CN-Cs also exhibit decreased decomposition of H<sub>2</sub>O<sub>2</sub>. The amine groups in the CN edge can operate as active sites for H<sub>2</sub>O<sub>2</sub> breakdown, which explains the aforementioned results [35]. However, CN-Cs demonstrates apparent H<sub>2</sub>O<sub>2</sub> decomposition when compared to CN-Li, CN-Na, CN-Rb, and CN-K, which may occur because the strong Lewis acid sites contribute to the H<sub>2</sub>O<sub>2</sub> activation [36].

#### 2.4. Mechanism

The mechanistic details for photocatalytic H<sub>2</sub>O<sub>2</sub> production for various specimens were explored. First, from the results of XRD patterns, it could be inferred that CN-Rb and CN-Cs with poly(heptazine imide) structure have excellent activity. CN-Li also has a similar structure. However, its performance is poor, indicating that poly(heptazine imide) structure is not the fundamental factor affecting the performance. In addition, the structure of CN-K is different from CN-Rb. However, its photocatalytic H<sub>2</sub>O<sub>2</sub> activity is excellent, which means that crystal structure is not the key element influencing the photocatalytic activity.

TPD-NH<sub>3</sub> and TPD-O<sub>2</sub> tests on acquired samples were conducted to further investigate the mechanism of photocatalytic H<sub>2</sub>O<sub>2</sub> synthesis. Figure 6a demonstrates that all of the CN-M display greater NH<sub>3</sub> desorption temperatures when compared to CN, indicating that the Lewis acidic sites in CN-M—particularly CN-K, CN-Rb, and CN-Cs—are more potent. Meanwhile, the adsorbed NH<sub>3</sub> quantity of the sample is listed in Table S3; the adsorbed NH<sub>3</sub> quantities of CN-K, CN-Rb, and CN-Cs are 0.58, 0.72, and 1.35 mmol/g, respectively—significantly increased compared to CN (0.38 mmol/g). The increased adsorbed NH<sub>3</sub> quantities indicate that more Lewis acidic sites are formed with the enhanced metallic character of alkali metal. Alcohol may be adsorbed onto CN and CN-Rb with adsorption energies of 1.11 and 3.16 eV, respectively, as suggested by the outcome of the DFT calculation (Figure S11e,f). This finding suggests that the increased Lewis acidic sites are involved in the alcohol adsorption process. As is common knowledge, oxygen adsorption on the catalyst surface is essential for ORR. Consequently, TPD-O<sub>2</sub> data (Figure 6b and Table S3) showed that CN showed an O<sub>2</sub> desorption peak at 123 °C with 13.18 mol/g, whereas the desorption temperature and amount of CN-M adsorbed underwent an increase. This shows that CN-M has good chemisorption capacity and capability of O<sub>2</sub> adsorption. In particular, the adsorbed O<sub>2</sub> amounts for CN-Rb and CN-Cs are 97.47 and 112.47 mol/g, respectively. Furthermore, the DFT calculation showed that the energies of adsorption onto CN and CN-Rb were −0.77 and −3.38 eV, respectively (Figure S11c,d), which agrees well with the TPD-O<sub>2</sub> results. Moreover, to further explore the change in oxygen content in the reaction liquid during the reaction process, the dissolved oxygen (DO) values in the reaction mixture were determined. The DO values of CN-M samples, particularly CN-Rb and CN-Cs, fell after stirring for 30 min in the dark, as shown in Figure S12a, indicating that a significant amount of oxygen was transferred from the solution to the catalyst surface. At the beginning of illumination, the DO values of CN-K, CN-Rb, and CN-Cs decreased sharply, corresponding to their excellent photocatalytic H<sub>2</sub>O<sub>2</sub> production. After 45 min, their DO values tended to remain constant. The equilibrium between dissolution and consumption, which indicates that the reaction system may swiftly add oxygen

derived from air to the reaction, is the cause of the DO value's tendency to balance when compared to the photocatalytic  $\text{H}_2\text{O}_2$  production. Additionally, an intriguing phenomenon was observed: relative to the initial DO, the DO rose after stirring for 5 min in the dark, as shown in Figure S13, and the D-values for various catalysts agree with the TPD- $\text{O}_2$  results. For TPD- $\text{O}_2$  results, CN-Cs has the highest adsorbed  $\text{O}_2$  quantity, and for DO, it also has the highest D-value. Meanwhile, the DO values of the closed system with catalyst degassing treatment were also tested (Figure S12b). It can be seen that as the reaction proceeds, the DO of CN-M gradually decreases, especially for CN-K, CN-Rb, and CN-Cs. Therefore, with the increased metallic character of alkali metals, the modified CN-M exhibits excellent alcohol and oxygen adsorption, which is favorable to photocatalytic  $\text{H}_2\text{O}_2$  production.

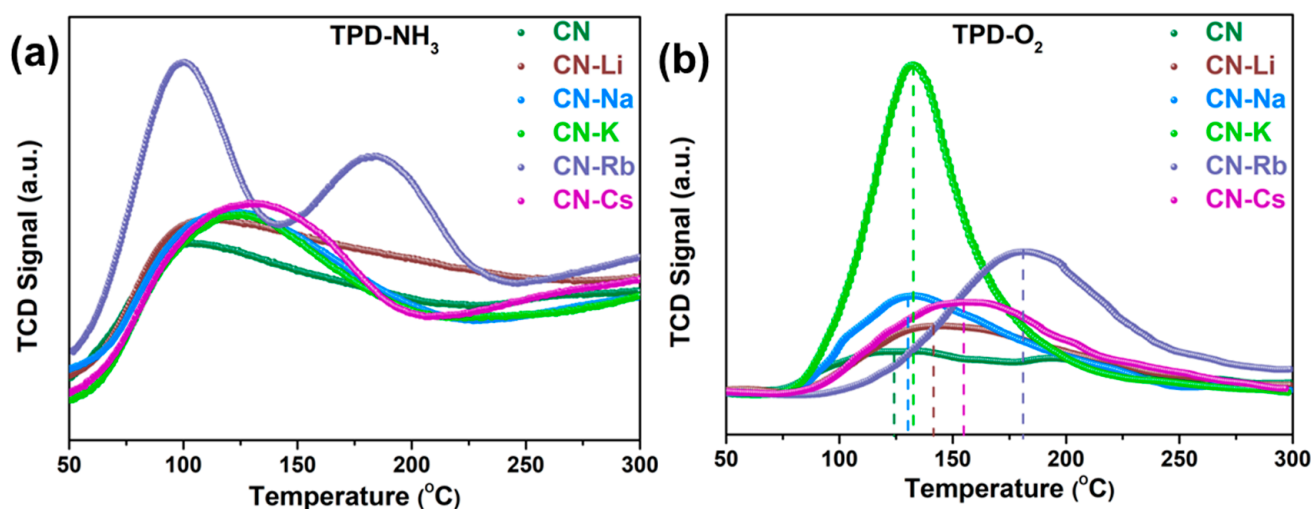
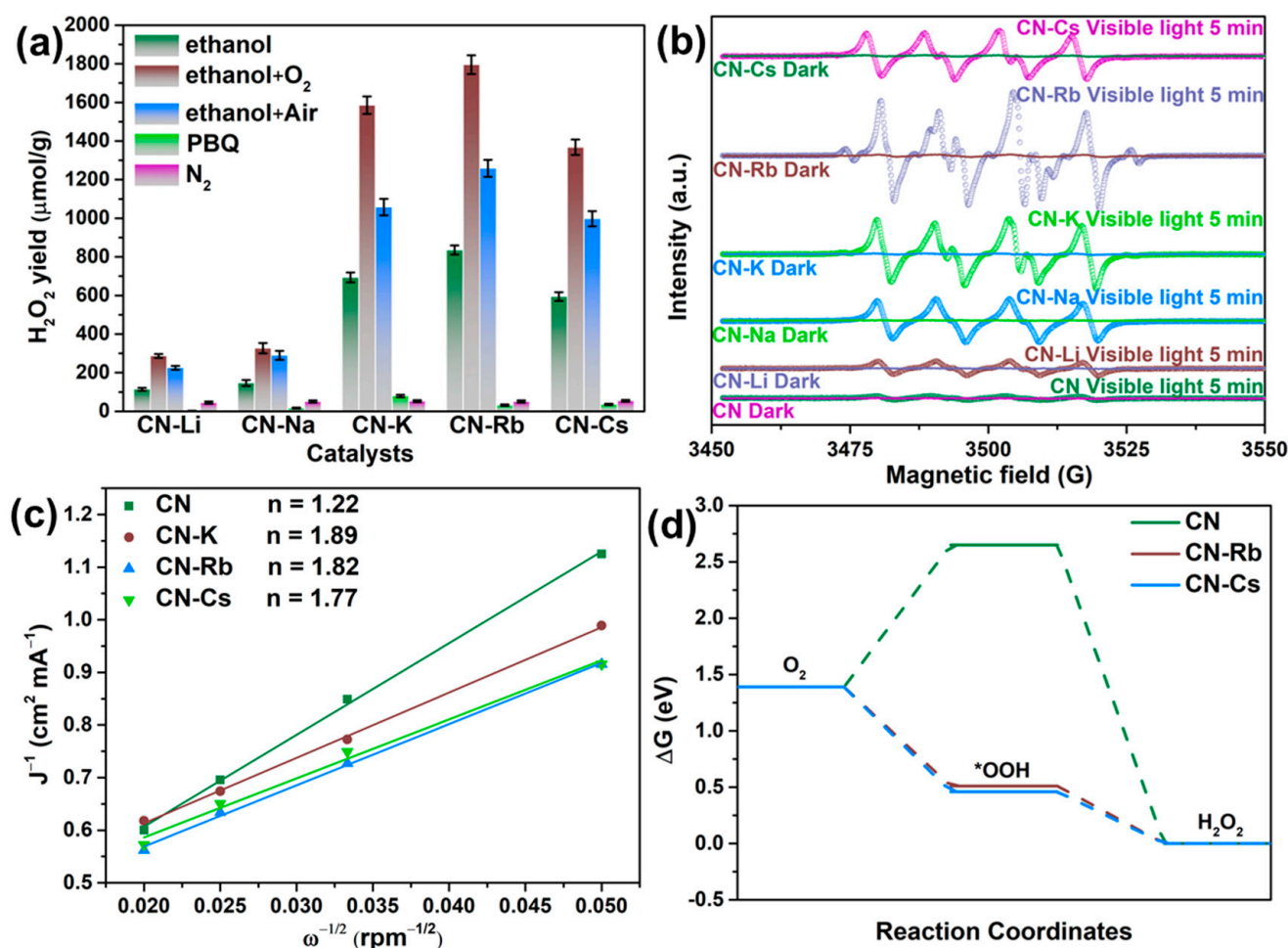


Figure 6. (a) TPD- $\text{NH}_3$  and (b) TPD- $\text{O}_2$  on the obtained PCN.

Various reaction settings were used to examine the CN-M sample's reaction pathway (as shown in Figure 7a). The photocatalytic synthesis of  $\text{H}_2\text{O}_2$  was carried out in nitrogen—that is, the reaction bottle was sealed after 5 min of  $\text{N}_2$  being injected into the system to replace  $\text{O}_2$ . The  $\text{H}_2\text{O}_2$  yields for the  $\text{N}_2$  atmosphere of CN-M were significantly reduced, as shown in Figure 7a. The  $\text{H}_2\text{O}_2$  yield increased visibly when  $\text{O}_2$  or air was fed into the reaction system, demonstrating that  $\text{O}_2$  was essential to the process. Additionally, a radical-capture experiment was carried out using *p*-benzoquinone (PBQ) as a superoxide radical-trapping agent. The findings demonstrate that superoxide radicals were essential for the photocatalytic generation of  $\text{H}_2\text{O}_2$  using PCN since the  $\text{H}_2\text{O}_2$  yields were significantly reduced. Additionally, the spin-trapping ESR/DMPO approach has proven the formation of superoxide radicals (as shown in Figure 7b) [37]. When exposed to visible light, which also identified the superoxide radical intermediates, the signal of DMPO/ $\bullet\text{OOH}$  of CN-M is noticeably higher in comparison to that of CN. Therefore, the two-step single-electron ORR pathway may represent the CN-M's reaction pathway.

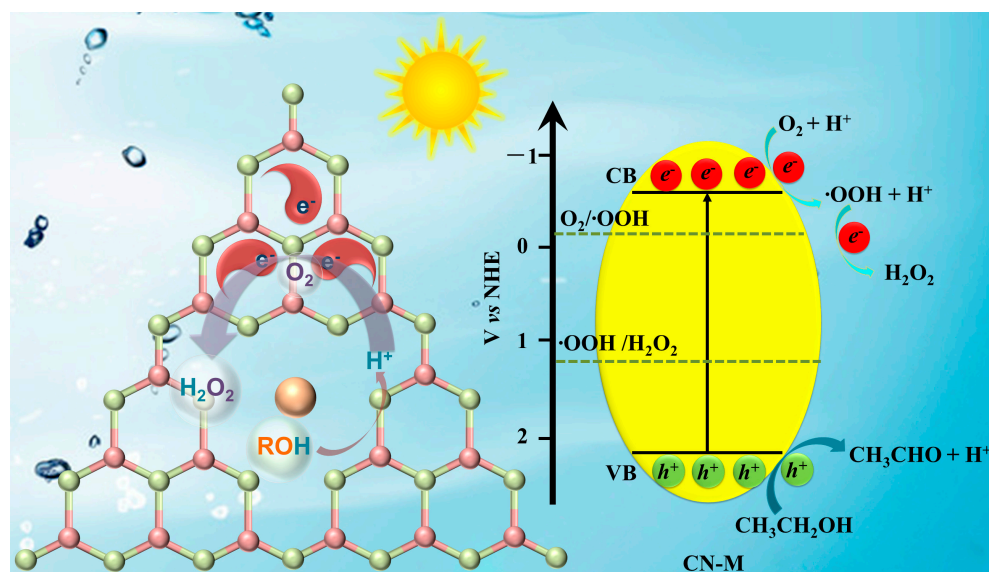
Additionally, the electron transfer number ( $n$ ) and kinetic current density ( $J_K$ ) in the ORR routes on the PCN samples were assessed through LSV in accordance with the Koutecky–Levich equation to further demonstrate that the reaction followed the  $2e^-$ -ORR pathway. The current densities of CN-K, CN-Rb, and CN-Cs were much higher than those of CN, as shown in Figures 7c and S15, showing that they had better oxygen-reduction activities than CN. Moreover, the values of  $n$  were 1.22, 1.89, 1.82, and 1.77 for CN, CN-K, CN-Rb, and CN-Cs, respectively, indicating that two-step single-electron ORR occurred on CN-K, CN-Rb, and CN-Cs.



**Figure 7.** (a) Photocatalytic production of H<sub>2</sub>O<sub>2</sub> employing the modified PCN under various conditions. (b) Electron paramagnetic resonance signal of DMPO/•OOH over the obtained PCN. (c) The average number of folds-transferred electrons (n). (d) The changes in the estimated Gibbs free energy of reduction of adsorbed O<sub>2</sub> to H<sub>2</sub>O<sub>2</sub>.

DFT calculations were performed to understand the H<sub>2</sub>O<sub>2</sub>-generation mechanism on PCN. A typical 2e<sup>-</sup>-ORR pathway was proposed as the route by which oxygen was photocatalytically reduced to H<sub>2</sub>O<sub>2</sub> [38]. Figure 7d demonstrates that CN-Rb and CN-Cs had lower G values during the •OOH production stage (0.51 and 0.46 eV, respectively) than CN (2.65 eV). The activated O<sub>2</sub> on CN-Rb and CN-Cs appeared to be converted more readily to •OOH based on the lower G values of •OOH production. The fact that adding Rb and Cs ions to PCN increased its kinetic activity was corroborated by the lower G of the protonation step for CN-Rb and CN-Cs.

In conclusion, Scheme 1 can be used to comprehend the processes that lead to the photocatalytic oxidation of ethanol and the creation of H<sub>2</sub>O<sub>2</sub> on CN-M. The photogenerated electrons were distributed on the N and C atoms (Figure S16b). At Lewis acidic sites, ethanol might be oxidized and adsorbed simultaneously. H<sub>2</sub>O<sub>2</sub> was produced when the adsorbed O<sub>2</sub> reacted with the special C and N atoms with two electrons.



**Scheme 1.** Proposed mechanism of photocatalytic  $\text{H}_2\text{O}_2$  production on CN-M.

### 3. Methods and Materials

#### 3.1. Materials

The Shanghai Macklin Biochemical Co. Ltd. (Shanghai, China) supplied the dicyandiamide (DCDA). Salts including, LiCl, NaCl, KCl, RbCl, and CsCl, were provided by the Saan Chemical Technology Co. Ltd. (Shanghai, China).

#### 3.2. Synthesis of CN-M

DCDA (5 g) and MCl (LiCl, NaCl, KCl, RbCl, or CsCl) were added into 50 mL beakers with 30 mL distilled water and heated at 80 °C for 2 h while stirring. After drying at 80 °C in an oven overnight, a white powder was heated at 550 °C for 4 h (4 °C/min) in a muffle furnace. After natural cooling to room temperature, the yellow solid was ground and filtered three times with boiling water and ethanol. After drying at 80 °C overnight, the modified PCN was obtained and named CN-M (M: Li, Na, K, Rb, Cs).

#### 3.3. Synthesis of CN

DCDA was directly heated at 550 °C for 4 h at a heating rate of 4 °C/min in a muffle furnace to act as a control, and the obtained PCN was named CN.

#### 3.4. Synthesis of Melem-M

DCDA was directly heated at 425 °C for 4 h at a heating rate of 4 °C/min in a muffle furnace. After cooling to room temperature, the sample was ground and named melem. Melem (1 g) and MCl (LiCl, NaCl, KCl, RbCl, or CsCl) were ground, mixed and heated at 550 °C for 2 h at a heating rate of 4 °C/min in a muffle furnace. After cooling to room temperature, the sample was filtered three times with distilled water and ethanol. After drying at 80 °C overnight, a yellow powder was obtained and named melem-M (M: Li, Na, K, Rb, Cs).

#### 3.5. Photocatalytic Production of $\text{H}_2\text{O}_2$

First, the photocatalytic  $\text{H}_2\text{O}_2$ -production properties of the obtained samples were screened on a multipass light catalytic reaction system (Perfectlight PCX50C Discover, Beijing, China) under white LED irradiation. Briefly, 0.03 g of the photocatalyst was adequately dispersed in 50 mL of an ethanol solution (10 vol%), after which the solution was irradiated under white LED light. The photocatalytic reaction was performed for 1 h with a 15-min interval for sample collection. The  $\text{H}_2\text{O}_2$  concentration was determined by

the colorimetric method, which is based on the peroxidase (POD)-catalyzed oxidation of *N,N*-diethyl-*p*-phenylenediamine (DPD) by hydrogen peroxide [16].

In order to further analyze the performance of samples, the photocatalytic H<sub>2</sub>O<sub>2</sub> production was measured employing a 350 W Xe lamp comprising a 420 nm UV filter (Perfectlight PLS-SXE300D, Beijing, China). Namely, 0.05 g of each sample was dispersed in 200 mL of aqueous ethanol (10 vol%). The photocatalytic process was performed for 12 h with an interval of 1 h for sample collection. The H<sub>2</sub>O<sub>2</sub> concentration was subsequently measured using the colorimetric method.

#### 4. Conclusions

Using thermal copolymerization with Li, Na, K, Rb, or Cs, alkali metal (M)-doped PCN was created and used to generate H<sub>2</sub>O<sub>2</sub> under the illumination of white LEDs. According to a comprehensive analysis, the activity of CN-M enhanced with the increase of the metallic character of alkali metals. The higher metallic character will give rise to stronger Lewis acidic sites. Although the strong Lewis acidic sites are helpful for the adsorption and activation of ethanol, they will also act as the activation sites of H<sub>2</sub>O<sub>2</sub> and enhance the self-degradation of H<sub>2</sub>O<sub>2</sub>. Hence, even though CN-Cs have the strongest oxygen adsorption capacity and the strongest and the highest number of Lewis acid sites, their photocatalytic performance for H<sub>2</sub>O<sub>2</sub> production is not optimal because of their strongest H<sub>2</sub>O<sub>2</sub> self-degradation activity. CN-Rb, on the other hand, has the best photocatalytic activity for H<sub>2</sub>O<sub>2</sub> production due to its suitable metallic character. This work presents a useful foundation for further exploring the photocatalytic reaction of metal-ion-modified PCN.

**Supplementary Materials:** The following supporting information can be downloaded at: <https://www.mdpi.com/article/10.3390/catal13020218/s1>, Figure S1: SEM images of obtained PCN: (a) CN, (b) CN-Li, (c) CN-Na, (d) CN-K, (e) CN-Rb, (f) CN-Cs, Figure S2: (a) N<sub>2</sub> adsorption-desorption isotherms. (b) the pore size distribution curves of the obtained PCN, Figure S3: XRD pattern of CN-Li-0.5, Figure S4: (a) XPS survey of obtained PCN. (b) High-resolution XPS spectra of C 1s of obtained PCN. (c) High-resolution XPS spectra of N 1s of obtained PCN. (d) High-resolution XPS spectra of O 1s of obtained PCN, Figure S5: Digital images of contact angle tests for PCN, Figure S6: The photographs of CN and CN-M dispersed in deionized water for 7 days, Figure S7: The chemical structures of CN and CN-M, Figure S8: Mott-Schottky plots over 500 Hz in 0.5 M Na<sub>2</sub>SO<sub>4</sub> and 0.2 M phosphate buffer electrolyte, Figure S9: Time-dependent change in H<sub>2</sub>O<sub>2</sub> evolution during photoreaction with PCN under visible light ( $\lambda > 420$  nm), Figure S10: Time-dependent change in H<sub>2</sub>O<sub>2</sub> evolution during photoreaction with PCN under visible light ( $\lambda > 420$  nm), Figure S11: The DFT calculations for CN and CN-Rb. Polymeric models for CN (a) and CN-Rb (b); The adsorption energies onto CN (c) and CN-Rb (d) for oxygen; The adsorption energies onto CN (e) and CN-Rb (f) for ethanol, Figure S12: The dissolved oxygen (DO) concentrations of reaction solution for the obtained PCN and without catalyst, Figure S13: The D-value of the initial DO and the DO after stirring 5 min for the obtained PCN, Figure S14: The DO test device with closed system, Figure S15: LSV curves of (a) CN, (b) CN-K, (c) CN-Rb, and (d) CN-Cs were measured on an RDE at different rotating speeds, Figure S16: Electronic structures of polymeric models for (a) CN and (b) CN-Rb together with their optimized HOMO and LUMO, Figure S17: The effect of solution pH on the decomposition of H<sub>2</sub>O<sub>2</sub> for CN-Rb under LED white light, Table S1: Physicochemical properties of the as-prepared samples, Table S2: XPS peak area ratio of the as-prepared samples, Table S3: TPD values of obtained PCN. References [39–43] are cited in the supplementary materials.

**Author Contributions:** Z.L. conceived, designed and performed the experiments; Y.C. analyzed the data and wrote the paper. All authors have read and agreed to the published version of the manuscript.

**Funding:** This work was financially supported by GDAS' Project of Science and Technology Development [2018GDASCX-0922/23].

**Data Availability Statement:** The data presented in this study are available on request from the corresponding author.

**Conflicts of Interest:** The authors declare no conflict of interest.

## References

1. Fuku, K.; Miyase, Y.; Miseki, Y.; Funaki, T.; Gunji, T.; Sayama, K. Photoelectrochemical Hydrogen Peroxide Production from Water on a  $\text{WO}_3/\text{BiVO}_4$  Photoanode and from  $\text{O}_2$  on an Au Cathode Without External Bias. *Chem. Asian J.* **2017**, *12*, 1111–1119. [[CrossRef](#)] [[PubMed](#)]
2. Pi, L.; Cai, J.; Xiong, L.; Cui, J.; Hua, H.; Tang, D.; Mao, X. Generation of  $\text{H}_2\text{O}_2$  by on-site activation of molecular dioxygen for environmental remediation applications: A review. *Chem. Eng. J.* **2020**, *389*, 123420–123436. [[CrossRef](#)]
3. Siahrostami, S.; Verdaguer-Casadevall, A.; Karamad, M.; Deiana, D.; Malacrida, P.; Wickman, B.; Escudero-Escribano, M.; Paoli, E.A.; Frydendal, R.; Hansen, T.W.; et al. Enabling direct  $\text{H}_2\text{O}_2$  production through rational electrocatalyst design. *Nat. Mater.* **2013**, *12*, 1137–1143. [[CrossRef](#)] [[PubMed](#)]
4. Theerthagiri, J.; Lee, S.J.; Karuppasamy, K.; Arulmani, S.; Veeralakshmi, S.; Ashokkumar, M.; Choi, M.Y. Application of advanced materials in sonophotocatalytic processes for the remediation of environmental pollutants. *J. Hazard. Mater.* **2021**, *412*, 125245. [[CrossRef](#)] [[PubMed](#)]
5. Moon, G.-h.; Kim, W.; Bokare, A.D.; Sung, N.-e.; Choi, W. Solar production of  $\text{H}_2\text{O}_2$  on reduced graphene oxide– $\text{TiO}_2$  hybrid photocatalysts consisting of earth-abundant elements only. *Energy Environ. Sci.* **2014**, *7*, 4023–4028. [[CrossRef](#)]
6. Xiong, X.; Zhang, X.; Liu, S.; Zhao, J.; Xu, Y. Sustained production of  $\text{H}_2\text{O}_2$  in alkaline water solution using borate and phosphate-modified Au/ $\text{TiO}_2$  photocatalysts. *Photochem. Photobiol. Sci.* **2018**, *17*, 1018–1022. [[CrossRef](#)]
7. Li, Y.; Ma, F.; Zheng, L.; Liu, Y.; Wang, Z.; Wang, P.; Zheng, Z.; Cheng, H.; Dai, Y.; Huang, B. Boron containing metal-organic framework for highly selective photocatalytic production of  $\text{H}_2\text{O}_2$  by promoting two-electron  $\text{O}_2$  reduction. *Mater. Horiz.* **2021**, *8*, 2842–2850. [[CrossRef](#)]
8. Fuku, K.; Takioka, R.; Iwamura, K.; Todoroki, M.; Sayama, K.; Ikenaga, N. Photocatalytic  $\text{H}_2\text{O}_2$  production from  $\text{O}_2$  under visible light irradiation over phosphate ion-coated Pd nanoparticles-supported  $\text{BiVO}_4$ . *Appl. Catal. B Environ.* **2020**, *272*, 119003–119010. [[CrossRef](#)]
9. Wang, K.; Li, Y.; Shi, H.; Chen, F.; Wang, P.; Wang, X. Optimizing Oxygen and Intermediate  $\text{HOO}^*$  Adsorption of Cu–Pd Alloy Cocatalyst for Boosting Photocatalytic  $\text{H}_2\text{O}_2$  Production of  $\text{BiVO}_4$ . *Adv. Sustain. Syst.* **2022**, *6*, 2200144. [[CrossRef](#)]
10. Shiraishi, Y.; Kanazawa, S.; Kofuji, Y.; Sakamoto, H.; Ichikawa, S.; Tanaka, S.; Hirai, T. Sunlight-driven hydrogen peroxide production from water and molecular oxygen by metal-free photocatalysts. *Angew. Chem. Int. Ed.* **2014**, *53*, 13454–13459. [[CrossRef](#)]
11. Shiraishi, Y.; Kanazawa, S.; Sugano, Y.; Tsukamoto, D.; Sakamoto, H.; Ichikawa, S.; Hirai, T. Highly selective production of hydrogen peroxide on graphitic carbon nitride (g- $\text{C}_3\text{N}_4$ ) photocatalyst activated by visible light. *ACS Catal.* **2014**, *4*, 774–780. [[CrossRef](#)]
12. Tang, R.; Gong, D.; Zhou, Y.; Deng, Y.; Feng, C.; Xiong, S.; Huang, Y.; Peng, G.; Li, L.; Zhou, Z. Unique g- $\text{C}_3\text{N}_4$ /PDI-g- $\text{C}_3\text{N}_4$  homojunction with synergistic piezo-photocatalytic effect for aquatic contaminant control and  $\text{H}_2\text{O}_2$  generation under visible light. *Appl. Catal. B Environ.* **2022**, *303*, 120929. [[CrossRef](#)]
13. Zhang, X.; Ma, P.; Wang, C.; Gan, L.; Chen, X.; Zhang, P.; Wang, Y.; Li, H.; Wang, L.; Zhou, X.; et al. Unraveling the dual defect sites in graphite carbon nitride for ultra-high photocatalytic  $\text{H}_2\text{O}_2$  evolution. *Energy Environ. Sci.* **2022**, *15*, 830–842. [[CrossRef](#)]
14. Yang, Q.; Li, R.; Wei, S.; Yang, R. Schottky functionalized Z-scheme heterojunction photocatalyst  $\text{Ti}_2\text{C}_3/\text{g-C}_3\text{N}_4/\text{BiOCl}$ : Efficient photocatalytic  $\text{H}_2\text{O}_2$  production via two-channel pathway. *Appl. Surf. Sci.* **2022**, *572*, 151525–151535. [[CrossRef](#)]
15. Zhang, X.; Yu, J.; Macyk, W.; Wageh, S.; Al-Ghamdi, A.A.; Wang, L.  $\text{C}_3\text{N}_4$ /PDA S-Scheme Heterojunction with Enhanced Photocatalytic  $\text{H}_2\text{O}_2$  Production Performance and Its Mechanism. *Adv. Sustain. Syst.* **2022**, 2200113. [[CrossRef](#)]
16. Zhao, Y.; Zhang, P.; Yang, Z.; Li, L.; Gao, J.; Chen, S.; Xie, T.; Diao, C.; Xi, S.; Xiao, B.; et al. Mechanistic analysis of multiple processes controlling solar-driven  $\text{H}_2\text{O}_2$  synthesis using engineered polymeric carbon nitride. *Nat. Commun.* **2021**, *12*, 3701–3711. [[CrossRef](#)] [[PubMed](#)]
17. Zhang, J.; Yu, C.; Lang, J.; Zhou, Y.; Zhou, B.; Hu, Y.H.; Long, M. Modulation of Lewis acidic-basic sites for efficient photocatalytic  $\text{H}_2\text{O}_2$  production over potassium intercalated tri-s-triazine materials. *Appl. Catal. B Environ.* **2020**, *277*, 119225–119233. [[CrossRef](#)]
18. Wang, Y.; Meng, D.; Zhao, X. Visible-light-driven  $\text{H}_2\text{O}_2$  production from  $\text{O}_2$  reduction with nitrogen vacancy-rich and porous graphitic carbon nitride. *Appl. Catal. B Environ.* **2020**, *273*, 119064–119072. [[CrossRef](#)]
19. Wu, S.; Yu, H.; Chen, S.; Quan, X. Enhanced Photocatalytic  $\text{H}_2\text{O}_2$  Production over Carbon Nitride by Doping and Defect Engineering. *ACS Catal.* **2020**, *10*, 14380–14389. [[CrossRef](#)]
20. Zhang, H.; Jia, L.; Wu, P.; Xu, R.; He, J.; Jiang, W. Improved  $\text{H}_2\text{O}_2$  photogeneration by KOH-doped g- $\text{C}_3\text{N}_4$  under visible light irradiation due to synergistic effect of N defects and K modification. *Appl. Surf. Sci.* **2020**, *527*, 146584–146594. [[CrossRef](#)]
21. Liu, W.; Wang, P.; Chen, J.; Gao, X.; Che, H.; Liu, B.; Ao, Y. Unraveling the Mechanism on Ultrahigh Efficiency Photocatalytic  $\text{H}_2\text{O}_2$  Generation for Dual-Heteroatom Incorporated Polymeric Carbon Nitride. *Adv. Funct. Mater.* **2022**, *32*, 2205119. [[CrossRef](#)]
22. Chen, L.; Chen, C.; Yang, Z.; Li, S.; Chu, C.; Chen, B. Simultaneously Tuning Band Structure and Oxygen Reduction Pathway toward High-Efficient Photocatalytic Hydrogen Peroxide Production Using Cyano-Rich Graphitic Carbon Nitride. *Adv. Funct. Mater.* **2021**, *31*, 2105731–2105740. [[CrossRef](#)]
23. Guo, Y.R.; Liu, Q.; Li, Z.H.; Zhang, Z.G.; Fang, X.M. Enhanced photocatalytic hydrogen evolution performance of mesoporous graphitic carbon nitride co-doped with potassium and iodine. *Appl. Catal. B Environ.* **2018**, *221*, 362–370. [[CrossRef](#)]
24. Wang, J.; Zhao, H.; Zhu, B.; Larter, S.; Cao, S.; Yu, J.; Kibria, M.G.; Hu, J. Solar-Driven Glucose Isomerization into Fructose via Transient Lewis Acid–Base Active Sites. *ACS Catal.* **2021**, *11*, 12170–12178. [[CrossRef](#)]

25. Pan, Z.; Zhao, M.; Zhuzhang, H.; Zhang, G.; Anpo, M.; Wang, X. Gradient Zn-Doped Poly Heptazine Imides Integrated with a van der Waals Homo Junction Boosting Visible Light-Driven Water Oxidation Activities. *ACS Catal.* **2021**, *11*, 13463–13471. [[CrossRef](#)]
26. Guo, F.; Hu, B.; Yang, C.; Zhang, J.; Hou, Y.; Wang, X. On-Surface Polymerization of In-Plane Highly Ordered Carbon Nitride Nanosheets toward Photocatalytic Mineralization of Mercaptan Gas. *Adv. Mater.* **2021**, *33*, 2101466–2101472. [[CrossRef](#)] [[PubMed](#)]
27. Liu, Q.; Wang, X.L.; Yang, Q.; Zhang, Z.G.; Fang, X.M. A novel route combined precursor-hydrothermal pretreatment with microwave heating for preparing holey g-C<sub>3</sub>N<sub>4</sub> nanosheets with high crystalline quality and extended visible light absorption. *Appl. Catal. B Environ.* **2018**, *225*, 22–29. [[CrossRef](#)]
28. Lau, V.W.; Moudrakovski, I.; Botari, T.; Weinberger, S.; Mesch, M.B.; Duppel, V.; Senker, J.; Blum, V.; Lotsch, B.V. Rational design of carbon nitride photocatalysts by identification of cyanamide defects as catalytically relevant sites. *Nat. Commun.* **2016**, *7*, 12165–12174. [[CrossRef](#)]
29. Wang, X.L.; Liu, Q.; Yang, Q.; Zhang, Z.G.; Fang, X.M. Three-dimension g-C<sub>3</sub>N<sub>4</sub> aggregate composed of hollow bubbles with high activity for photocatalytic degradation of tetracycline. *Carbon* **2018**, *136*, 103–112. [[CrossRef](#)]
30. Li, Z.; Yang, Q.; Chen, C.; Zhang, Z.; Fang, X. Enhanced photocatalytic performance of polymeric C<sub>3</sub>N<sub>4</sub> doped with theobromine composed of an imidazole ring and a pyrimidine ring. *Chin. J. Catal.* **2019**, *40*, 875–885. [[CrossRef](#)]
31. Shen, R.; He, K.; Zhang, A.; Li, N.; Ng, Y.H.; Zhang, P.; Hu, J.; Li, X. In-situ construction of metallic Ni<sub>3</sub>C@Ni core-shell cocatalysts over g-C<sub>3</sub>N<sub>4</sub> nanosheets for shell-thickness-dependent photocatalytic H<sub>2</sub> production. *Appl. Catal. B Environ.* **2021**, *291*, 120104. [[CrossRef](#)]
32. Fu, J.; Zhu, B.; Jiang, C.; Cheng, B.; You, W.; Yu, J. Hierarchical Porous O-Doped g-C<sub>3</sub>N<sub>4</sub> with Enhanced Photocatalytic CO<sub>2</sub> Reduction Activity. *Small* **2017**, *13*, 1603938–1603946. [[CrossRef](#)]
33. Wang, C.; Fan, H.; Ren, X.; Ma, J.; Fang, J.; Wang, W. Hydrothermally induced O-doping and porous structure of graphitic carbon nitride with highly ordered architecture and dramatically enhanced photocatalytic property. *ChemSusChem* **2017**, *11*, 700–708. [[CrossRef](#)] [[PubMed](#)]
34. Wang, H.; Sun, X.; Li, D.; Zhang, X.; Chen, S.; Shao, W.; Tian, Y.; Xie, Y. Boosting Hot-Electron Generation: Exciton Dissociation at the Order-Disorder Interfaces in Polymeric Photocatalysts. *J. Am. Chem. Soc.* **2017**, *139*, 2468–2473. [[CrossRef](#)] [[PubMed](#)]
35. Mamba, G.; Mishra, A.K. Graphitic carbon nitride (g-C<sub>3</sub>N<sub>4</sub>) nanocomposites: A new and exciting generation of visible light driven photocatalysts for environmental pollution remediation. *Appl. Catal. B Environ.* **2016**, *198*, 347–377. [[CrossRef](#)]
36. Ahmad, M.; Quan, X.; Chen, S.; Yu, H. Tuning Lewis acidity of MIL-88B-Fe with mix-valence coordinatively unsaturated iron centers on ultrathin Ti<sub>3</sub>C<sub>2</sub> nanosheets for efficient photo-Fenton reaction. *Appl. Catal. B Environ.* **2020**, *264*, 118534–118545. [[CrossRef](#)]
37. Shen, R.; Zhang, L.; Li, N.; Lou, Z.; Ma, T.; Zhang, P.; Li, Y.; Li, X. W–N Bonds Precisely Boost Z-Scheme Interfacial Charge Transfer in g-C<sub>3</sub>N<sub>4</sub>/WO<sub>3</sub> Heterojunctions for Enhanced Photocatalytic H<sub>2</sub> Evolution. *ACS Catal.* **2022**, *12*, 9994–10003. [[CrossRef](#)]
38. Liu, B.; Du, J.; Ke, G.; Jia, B.; Huang, Y.; He, H.; Zhou, Y.; Zou, Z. Boosting O<sub>2</sub> Reduction and H<sub>2</sub>O Dehydrogenation Kinetics: Surface N-Hydroxymethylation of g-C<sub>3</sub>N<sub>4</sub> Photocatalysts for the Efficient Production of H<sub>2</sub>O<sub>2</sub>. *Adv. Funct. Mater.* **2021**, *32*, 2111125–2111136. [[CrossRef](#)]
39. Kresse, G.; Furthmüller, J. Efficiency of ab-initio total energy calculations for metals and semiconductors using a plane-wave basis set. *Comput. Mater. Sci.* **1996**, *6*, 15–50. [[CrossRef](#)]
40. Kresse, G.; Furthmüller, J. Efficient iterative schemes for ab initio total-energy calculations using a plane-wave basis set. *Phys. Rev. B* **1996**, *54*, 11169–11186. [[CrossRef](#)]
41. Perdew, J.P.; Burke, K.; Ernzerhof, M. Generalized gradient approximation made simple. *Phys. Rev. Lett.* **1996**, *77*, 3865. [[CrossRef](#)] [[PubMed](#)]
42. Perdew, J.P.; Ernzerhof, M.; Burke, K. Rationale for mixing exact exchange with density functional approximations. *J. Chem. Phys.* **1996**, *105*, 9982–9985. [[CrossRef](#)]
43. Kresse, G.; Joubert, D. From ultrasoft pseudopotentials to the projector augmented-wave method. *Phys. Rev. B* **1999**, *59*, 1758–1775. [[CrossRef](#)]

**Disclaimer/Publisher's Note:** The statements, opinions and data contained in all publications are solely those of the individual author(s) and contributor(s) and not of MDPI and/or the editor(s). MDPI and/or the editor(s) disclaim responsibility for any injury to people or property resulting from any ideas, methods, instructions or products referred to in the content.